Nanoscale

PAPER

View Article Online
View Journal | View Issue

Cite this: *Nanoscale*, 2024, **16**, 9382

An $IrRuO_x$ catalyst supported by oxygen-vacant Ta oxide for the oxygen evolution reaction and proton exchange membrane water electrolysis†

Yanrong Liu,[a,b,c] Meiqi Zhang,[c] Cong Zhang,[d] Honghua Zhang[c] and Hao Wang *[a,b,c]

The sustainable development of proton exchange membrane water electrolysis (PEMWE) requires a dramatic reduction in Ir while maintaining good catalytic activity and stability for the oxygen evolution reaction (OER). Herein, high-surface-area Ta_2O_5 with abundant oxygen vacancies is synthesized *via* a facile process, followed by anchoring $IrRuO_x$ onto a Ta_2O_5 support ($IrRuO_x/Ta_2O_5$). $IrRuO_x$ and Ta_2O_5 work synergistically to afford excellent catalytic performance for the acidic OER. At 0.3 mg_{Ir} cm^{-2}, $IrRuO_x/Ta_2O_5$ only needed an overpotential of 235 mV to deliver 10 mA cm^{-2} in an acidic half cell and needed a cell potential of 1.91 V to deliver 2 A cm^{-2} in a PEM water electrolyzer. The characterization results show that doping Ir into RuO_x significantly improves the stability and the electrochemically active surface area of RuO_x. In $IrRuO_x/Ta_2O_5$, $IrRuO_x$ interacts with Ta_2O_5 through more electron-rich Ir, indicating strong synergy between the catalyst and the support. The use of a metal oxide support improves the catalyst dispersion, optimizes electronic structures, facilitates mass transport, and stabilizes active sites. This work demonstrates that compositing Ir with less expensive Ru and anchoring catalyst nanoparticles on platinum-group metal (PGM)-free metal oxide supports represents one of the most promising strategies to reduce Ir loading and achieve an activity–stability trade-off. Such a strategy can benefit future catalyst design for other energy storage and conventional processes.

Received 5th December 2023,
Accepted 7th April 2024

DOI: 10.1039/d3nr06211b

rsc.li/nanoscale

1. Introduction

The development of hydrogen energy is critical for becoming a sustainable society.[1] As a raw material and an energy carrier, hydrogen can be used to decarbonize many sectors, such as industry, transportation, and power.[2] In hydrogen-driven scenarios, hydrogen production technology lays the foundation for determining whether hydrogen energy can be implemented at large scales.[3] Water electrolysis driven by renewable electricity is promising due to its high efficiency and emission-free nature.[4] In particular, proton exchange membrane water electrolysis (PEMWE) can produce highly pure hydrogen at a high current density and can work easily with intermittent renewable electricity.[5] Unfortunately, the anodic oxygen evolution reaction (OER) of PEMWEs is kinetically sluggish and requires a highly oxidative and acidic environment.[6] The current catalyst of choice uses a high loading of Ir, which has a lower crustal reserve than Pt and causes an extremely high cost hurdle for commercialization.[7,8] Therefore, reducing the Ir loading while maintaining the OER activity and stability is necessary for the sustainable development of PEMWEs.[9–11]

One popular strategy for developing low-Ir catalysts is alloying with Ru. Although Ru is also a platinum-group metal (PGM), it is much more affordable than Ir. In the acidic OER, Ru is more active but less stable than Ir;[12] thus, precisely controlling the IrRu composition can achieve an activity–stability trade-off.[13–15] However, carefully designed alloy nanoparticles always agglomerate into large clusters whose surface is unable to fully participate in the OER. To overcome this problem, cata-

[a]*Beijing Key Laboratory of Ionic Liquids Clean Process, CAS Key Laboratory of Green Process and Engineering, State Key Laboratory of Multiphase Complex Systems, Institute of Process Engineering, Chinese Academy of Sciences, Beijing 100190, China. E-mail: haowang@ipe.ac.cn*
[b]*School of Chemical Engineering, University of Chinese Academy of Sciences, Beijing 100049, China*
[c]*Longzihu New Energy Laboratory, Zhengzhou Institute of Emerging Industrial Technology, Henan University, Zhengzhou 450000, China*
[d]*SINOPEC Research Institute of Petroleum Processing Co., Ltd, Beijing 100083, China*

†Electronic supplementary information (ESI) available: Synchrotron and electrochemical experimental details, TEM images, element mapping images, BET surface area and pore volume summary, XPS and EDS elemental content summary, XPS O 1s peak summary, XPS Ru 3d fitting results, double layer capacitance, a photograph of CCM with gaskets, and comparison of OER catalytic performance with literature reports. See DOI: https://doi.org/10.1039/d3nr06211b

lyst supports are often introduced to better disperse nanoparticles and generate catalyst–support interactions to stabilize the active sites.[16,17] In particular, the PGM-free support in the anode will significantly reduce the PGM loading, thus improving the competitiveness of the PEMWE cost. Unfortunately, the harsh conditions of the acidic OER make it impossible to use conventional PGM-free supports with good electronic conductivity, such as carbonaceous materials and transition metals.[18] These supports will be oxidized or dissolved under working conditions. The dissolved transition metal ions penetrate the membrane under an electric field and block the proton transfer path. Therefore, finding stable and conductive PGM-free supports is quite meaningful but challenging.[19,20]

A few insightful studies have used Ti-, W-, and Sn-based oxides as PGM-free supports.[21–24] These oxides are relatively stable in acids, and the main idea behind using these supports is to construct metal–metal oxide interactions to modify the electronic structures and optimize binding energies with the oxygen intermediates.[25,26] Ta oxides are also attractive candidates for exploration due to their tunable electronic structures and excellent stability against corrosion and dissolution.[27] Recent studies demonstrated that oxygen-induced Ta_2O_5 [28] and Fe-doped Ta_2O_5 [29] have good OER activity in alkaline media, suggesting that they are active toward water oxidation. In terms of catalyst supports for the acidic OER, Xu and co-workers[30] designed an IrO_2–Ta_2O_5 anode and found that different calcination temperatures had a great impact on the exposed crystal plane of IrO_2. Amano and co-workers[31] coated Ti felt with amorphous IrO_2–Ta_2O_5 layers and found that the acidic OER activity was dependent on the calcination temperature. In a more recent study, Pak and co-workers[32] supported Ir with mesoporous Ta_2O_5 to improve Ir utilization, electronic conductivity, and the electrochemically active surface area. Despite these insightful studies, Ir supported by Ta oxides for the acidic OER still requires an overpotential of 300 mV at 10 mA cm^{-2} in half cells, and the loading of Ir is still higher than 0.5 mg_{Ir} cm^{-2} to achieve satisfactory single cell performance. Therefore, the potential of the Ta_2O_5 support to reduce Ir loading and achieve high catalytic activity has not yet been fully demonstrated.

Herein, we composited $IrRuO_x$ with Ta_2O_5 to reduce Ir loading and further improved the OER and PEMWE performance. The Ta_2O_5 support developed in this work was confirmed to be amorphous with a high surface area and a high concentration of oxygen vacancies, and such advantageous structures resulted in uniformly distributed $IrRuO_x$ with intimate contact. In the active $IrRuO_x$ phase, Ir atoms were doped into RuO_x and coupled with Ta to form strong interactions. As tested in half cells, at 0.03 mg_{Ir} cm^{-2}, the catalyst needed only a 284 mV overpotential to deliver 10 mA cm^{-2}. By improving to 0.3 mg_{Ir} cm^{-2}, $IrRuO_x$ only needed an overpotential of 235 mV to deliver 10 mA cm^{-2} in a half cell and needed a potential of 1.91 V to deliver 2 A cm^{-2} in a PEM water electrolyzer. The good dispersion of the catalyst with high utilization, the close contact between $IrRuO_x$ and Ta_2O_5, and the modified electronic structures of the active sites are responsible for the enhanced electrochemical performance.

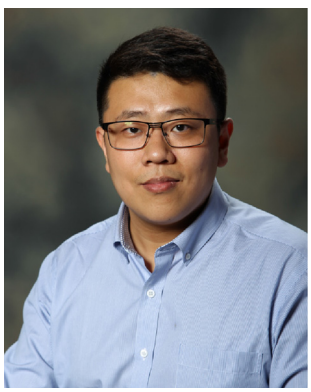

Hao Wang

Dr Hao Wang received his Ph.D. degree from the Beijing University of Chemical Technology in 2019. He was a guest graduate student at Argonne National Laboratory and a postdoctoral researcher at National Renewable Energy Laboratory. He is now a staff scientist in the Institute of Process Engineering, Chinese Academy of Sciences. His expertise includes rational design of electrocatalysts and membrane electrode assemblies in hydrogen fuel cells and water electrolyzers. He has published more than 30 papers in international journals such as Adv. Mater., ACS Energy Lett., Appl. Catal. B, Adv. Funct. Mater., etc.

2. Experimental

To synthesize the samples studied in this work, dihydrogen hexachloroiridate(IV) hydrate ($H_2IrCl_6{\cdot}6H_2O$, Ir ≥39%) was purchased from Sigma-Aldrich. Tantalum ethoxide ($C_{10}H_{25}O_5Ta$, 99.99%), ruthenium(III) chloride ($RuCl_3$, 99.5%, Ru: 47%), sodium borohydride ($NaBH_4$, ≥95%), ethylene glycol ($C_2H_6O_2$, >99.5), and tantalum oxide (Ta_2O_5, 99.99%) were purchased from Adamas-Beta. Ammonium fluoride (NH_4F, ≥98.0%) was purchased from Greagent. All chemicals were used as received, without further purification.

2.1 Synthesis of Ta_2O_5

To prepare Ta_2O_5, 0.3 g of tantalum ethoxide was dissolved in 6 mL of 0.1 M NH_4F in ethylene glycol. The resulting solution was mixed with 6 mL of water in an inner Teflon tube under rapid stirring, and the inner Teflon tube was sealed in a stainless-steel autoclave and placed in an oven. The oven was heated to 220 °C, maintained for 20 h, and naturally cooled to room temperature. The precipitate was collected by centrifugation and washed with water 3 times and then with ethanol 3 times to remove the unreacted residues. Ta_2O_5 powder was finally obtained after vacuum drying at 60 °C for 10 h.

2.2 Synthesis of $IrRuO_x/Ta_2O_5$

To composite $IrRuO_x$, Ta_2O_5, $RuCl_3$ hydrate, and H_3IrCl_6 with a mass ratio of 1/2.07/0.44 were dissolved in 10 mL of water to form solution A. In a subsequent step, 20 mg of $NaBH_4$ was dissolved in 6 mL of ice-cold water to form solution B. Solution B was then added to solution A, and the resulting mixture was magnetically stirred for 6 h at room temperature. After the reaction, the solid sample was collected by centrifu-

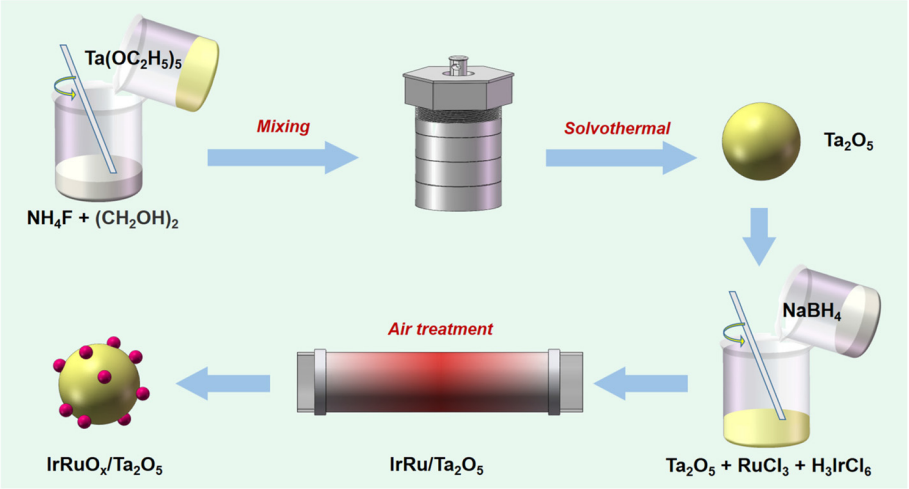

Scheme 1 Synthesis procedure for Ta_2O_5 and $IrRuO_x/Ta_2O_5$.

gation and washed with water 3 times and then with ethanol 3 times, followed by vacuum drying at 60 °C for 10 h. The $IrRuO_x/Ta_2O_5$ catalyst was finally obtained after heat treatment in a tube furnace, which was heated to 350 °C and maintained for 2 h under an air atmosphere. The overall process of catalyst synthesis is schematically shown in Scheme 1. For comparison, IrO_x/Ta_2O_5 and RuO_x/Ta_2O_5 were also prepared following the same synthesis procedure except for the addition of only Ru and Ir precursors, respectively. To study the PGM loadings and their impact on the acidic OER, $0.5IrRuO_x/Ta_2O_5$ (half Ir and Ru precursors added) and $1.5IrRuO_x/Ta_2O_5$ (1.5-fold Ir and Ru precursors added) were also prepared following the same synthesis procedure. The sample-C used in this work refers to a commercially available sample.

2.3 Materials characterization

The crystalline structures of the studied samples were examined using an X-ray diffractometer (XRD, Rigaku Co. Ltd, Japan) employing Cu Kα radiation (λ = 1.54056 Å) operated at 40 kV. A JEM-2100F high-resolution field-emission transmission electron microscope (FETEM, JEOL, Japan) and a SIGMA 500/VP scanning electron microscope (Zeiss, Germany) were used to observe the morphology of the samples. X-ray photoelectron spectroscopy (XPS) measurements were conducted on an EscaLab 250Xi spectrometer (Thermo Fisher Scientific, USA), and the spectra were processed by calibrating C 1s to 284.8 eV. The specific surface area was measured by N_2 adsorption–desorption at 77 K with an ASAP 2460 gas sorption analyzer (Micromeritics, USA). Bulk oxygen vacancy signals were detected by low temperature electron paramagnetic resonance (EPR, Bruker, EMXplus-6/1, Germany) under liquid nitrogen conditions, and the sample dosage was approximately 10 mg.

The experimental details for synchrotron and electrochemical characterization are available in the ESI.†

3. Results and discussion

3.1 Physical characterization of the catalysts

The crystalline structures of the prepared samples were determined by XRD. According to Fig. 1A, the diffraction peaks of the Ta sample developed in this work are indexed to Ta_2O_5 (JCPDS, PDF no. 08-0225). However, compared with commercial Ta_2O_5 powder (Ta_2O_5-C), Ta_2O_5 has broader diffraction peaks. After integration with the $IrRuO_x$ active species (Fig. 1B), all the Ta_2O_5 peaks were retained, with several new broad peaks emerging at (2θ=) 28.6°, 35.5°, and 54.5°. While IrO_2 (JCPDS, PDF no. 43-1019) and RuO_2 (JCPDS, PDF no. 43-1027) show similar XRD peak positions, the new peaks on Ta_2O_5 are closer to those of RuO_2, indicating that Ir is doped into the RuO_x phase.

The morphologies of the studied samples were observed by TEM. The Ta_2O_5 sample consists of sphere-like particles agglomerated into large clusters (Fig. 1C and Fig. S1, see the ESI†). There are no other notable features on its smooth surface. HRTEM further revealed the (210) lattice plane of Ta_2O_5 with a lattice spacing of 0.233 nm (Fig. 1c). After introducing the $IrRuO_x$ active species, $IrRuO_x/Ta_2O_5$ showed a bumpy surface, which was caused by $IrRuO_x$ growth on the Ta_2O_5 surface (Fig. 1D). However, no individual well-defined $IrRuO_x$ nanoparticles were observed, suggesting a uniform distribution of $IrRuO_x$ on the Ta_2O_5 substrate. HRTEM revealed a lattice spacing of 0.325 nm, which is assigned to the (110) lattice plane of RuO_2 but is larger than the standard value of RuO_2 (Fig. 1d). This was caused by Ir doping, which slightly expanded the lattice. To determine how the elements were distributed within the $IrRuO_x/Ta_2O_5$ sample, EDS was performed, and the resulting elemental mapping images are shown in Fig. 2. According to the images, Ta, Ir, Ru, and O are uniformly distributed, and $IrRuO_x$ and Ta_2O_5 are undistinguishable, which is evidence of intimate contact and synergy. Uniform element distributions were also observed for RuO_x/Ta_2O_5

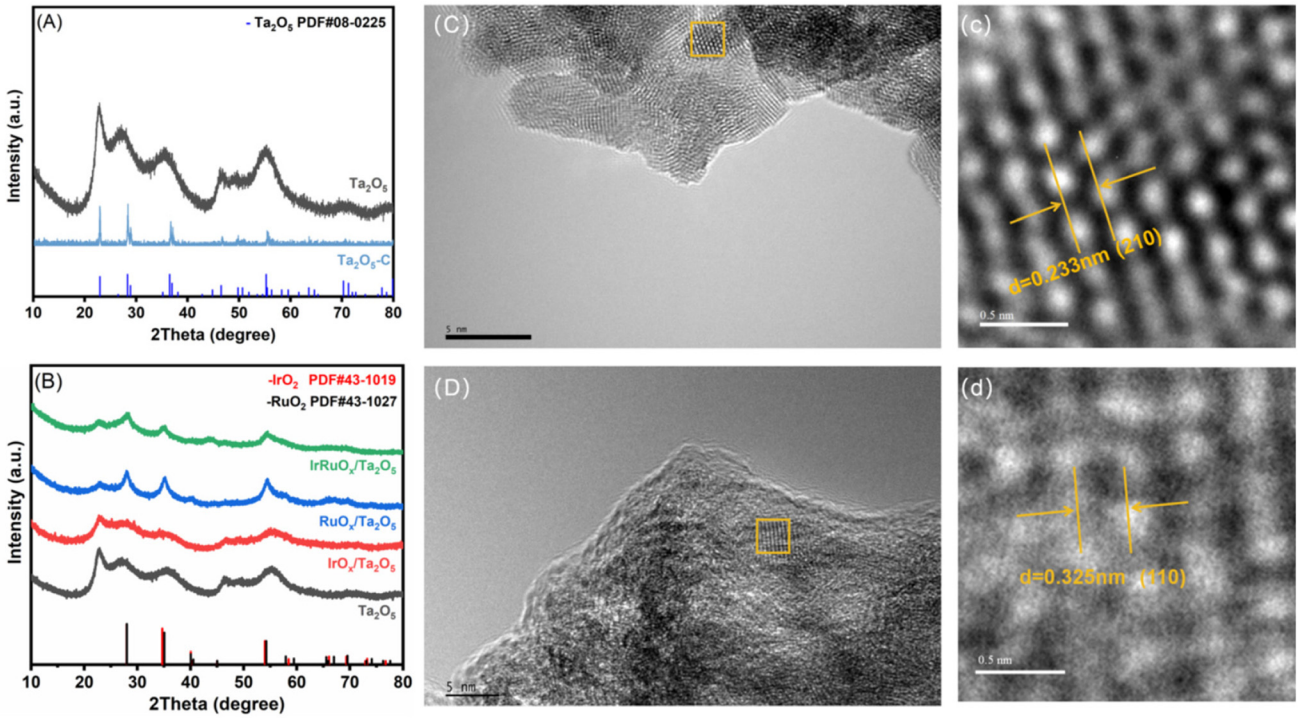

Fig. 1 (A) Comparison of XRD patterns between Ta_2O_5 and Ta_2O_5-C. (B) Comparison of XRD patterns between Ta_2O_5, IrO_x/Ta_2O_5, RuO_x/Ta_2O_5, and $IrRuO_x/Ta_2O_5$. (C) TEM image and (c) HRTEM image of Ta_2O_5. (D) TEM image and (d) HRTEM image of $IrRuO_x/Ta_2O_5$.

(Fig. S2, see the ESI†) and IrO_x/Ta_2O_5 (Fig. S3, see the ESI†). The atomic ratio of O/Ru/Ta/Ir in $IrRuO_x/Ta_2O_5$ was determined to be 69.68/16.45/11.75/2.12 by EDS. This ratio was used to determine the catalyst loading on the electrodes.

To assess the surface areas and pore structures, the studied samples were tested at 77 K for N_2 adsorption–desorption behavior. The resulting isotherms are displayed in Fig. 3A, and the parameters are summarized in Table S1 (see the ESI†). Notably, Ta_2O_5-C has little N_2 adsorption, and its BET surface area was determined to be extremely low at 2.92 $m^2\ g^{-1}$. By using the method developed in this work, the as-prepared Ta_2O_5 showed a much greater N_2 uptake, confirming its porous nature, and its BET surface area significantly improved to 231.56 $m^2\ g^{-1}$. Such a high surface area is favorable for Ta_2O_5 to serve as a catalyst support to confine the catalyst size and improve the catalyst dispersion. After integration with $IrRuO_x$, the $IrRuO_x/Ta_2O_5$ sample shows a decreased BET surface area of 98.18 $m^2\ g^{-1}$, suggesting that the $IrRuO_x$ nanoparticles are nonporous. Overall, owing to the highly porous Ta_2O_5 support, $IrRuO_x/Ta_2O_5$ still possesses a high surface area as an anode catalyst. To determine the pore structures in the studied samples, pore size distributions were plotted as shown in Fig. 3B. Unsurprisingly, Ta_2O_5-C has no pores. Ta_2O_5 and $IrRuO_x/Ta_2O_5$ have pores primarily distributed in widths ranging from 2 to 20 nm and 2 to 7 nm, respectively, confirming that they are both mesoporous. The pore volumes of Ta_2O_5 and $IrRuO_x/Ta_2O_5$ were determined to be 0.097 $cm^3\ g^{-1}$ and 0.043 $cm^3\ g^{-1}$, respectively (Table S1, see the ESI†). $IrRuO_x/Ta_2O_5$ also shows a small number of macropores with pore widths greater than 50 nm, which results from the stacking of the agglomerates. The abundant hierarchical pores of $IrRuO_x/Ta_2O_5$ will facilitate mass transport during the PEMWE.[33]

To gain further insight into the as-prepared Ta_2O_5 structure, EPR was conducted to examine the Ta–O coordination environment and the unpaired electrons. Ta_2O_5-C was also tested as a reference. As shown in Fig. 3C, Ta_2O_5-C shows a flight curve without any EPR response. However, Ta_2O_5 synthesized in this work has a high signal density, suggesting the existence of a high concentration of oxygen vacancies in Ta_2O_5. Abundant oxygen vacancies are usually favorable for catalyst growth and often result in interactions between the catalyst and support. Additionally, Ta oxides with oxygen vacancies are more electronically conductive than regular oxygen-saturated Ta_2O_5.[34] After compositing with $IrRuO_x$, the signal intensity decreased, but vacancies were still detectable in $IrRuO_x/Ta_2O_5$. Since Ta_2O_5 was fully covered by $IrRuO_x$ and underwent air treatment, the remaining oxygen vacancies also originated from $IrRuO_x$ clusters due to their high surface-to-volume ratios.[35]

The surface compositions of the studied samples were examined by XPS, and Ta, Ir, Ru, and O were all detected in the full spectrum of $IrRuO_x/Ta_2O_5$ (Fig. 3D). The atomic composition obtained by XPS is in good agreement with that obtained by EDS (Table S2, see the ESI†). Fig. 3E shows the deconvoluted Ta 4f spectra and the fitted results for Ta_2O_5-C, Ta_2O_5, and $IrRuO_x/Ta_2O_5$. The Ta 4f spectra for all three

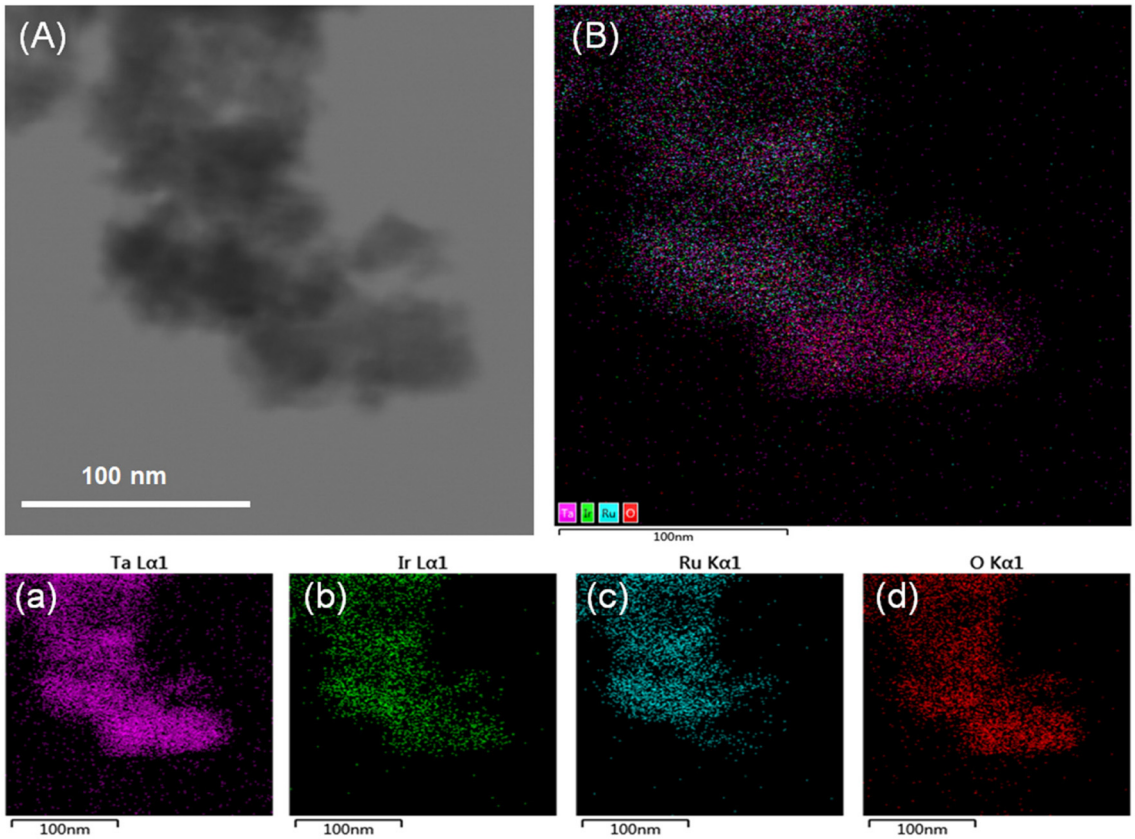

Fig. 2 (A) TEM image of the selected area to perform EDS. (B) Element mapping image with all elements overlapped. Individual element mapping of (a) Ta, (b) Ir, (c) Ru, and (d) O.

samples can be fitted into two peaks, with the one at a lower binding energy assigned to Ta $4f_{7/2}$ and the other to Ta $4f_{5/2}$.[36] Compared to Ta_2O_5-C, Ta_2O_5 developed in this work showed lower Ta 4f binding energies, indicating a lower Ta valence in Ta_2O_5, and the abundant oxygen vacancies in Ta_2O_5 were responsible for these results, as confirmed by the EPR experiments. After integration with $IrRuO_x$, the Ta 4f spectra of $IrRuO_x/Ta_2O_5$ retained similar features but showed slightly higher binding energies than those of Ta_2O_5. This is an indication of interactions between the PGM catalyst and the Ta_2O_5 support. Fig. 3F shows the deconvoluted Ir 4f spectra and the fitted results for $IrRuO_x/Ta_2O_5$ and commercial IrO_2 (IrO_2-C). Even though $IrRuO_x/Ta_2O_5$ was fully oxidized in air during its preparation, the Ir 4f spectra of $IrRuO_x/Ta_2O_5$ showed slightly lower binding energies compared to those of Ta_2O_5, confirming the strong interactions between the PGM catalyst and the Ta_2O_5 support. It can be concluded that Ir active sites were more electron-rich compared to IrO_2-C.[32,35] Ir with a lower valence state usually shows better sustainability with higher stability.[37] Fig. 3G shows the deconvoluted Ru 3p spectra and the fitted results for $IrRuO_x/Ta_2O_5$ and commercial RuO_2 (RuO_2-C). These two samples show similar peaks, indicating similar Ru valence states. No binding energy shifts were observed, which was not expected from the Ir results, indicating that interactions mainly occur between Ta and Ir. Fig. S4 (see the ESI†) shows a comparison of the Ru 3d spectra and the fitting results for $IrRuO_x/Ta_2O_5$ and RuO_x/Ta_2O_5. In the figure, Ru $3d_{5/2}$, Ru $3d_{3/2}$, and their satellite peaks were observed. The other three peaks are related to carbon species. However, the Ru $3d_{5/2}$ and Ru $3d_{3/2}$ binding energies of $IrRuO_x/Ta_2O_5$ were positively shifted (~0.1 eV) compared to those of RuO_x/Ta_2O_5, suggesting that the Ru in $IrRuO_x/Ta_2O_5$ had a higher oxidation state. Previous studies have indicated that a higher valence state of Ru is more favorable for the OER.[38,39]

Since the oxygen electronic structures are critical in this study, we further fitted the deconvoluted O 1s spectra as shown in Fig. 3H, and the resulting parameters are summarized in Table S3 (see the ESI†). To understand the differences between the individual components, Ta_2O_5-C, IrO_2-C, and RuO_2-C were also tested as references. The O 1s spectra of Ta_2O_5-C can be fitted by four peaks centered at 530.0 eV, 531.1 eV, 532.1 eV, and 533.2 eV, which are assigned to lattice O, vacant O, water, and adventitious species, respectively. For the Ta_2O_5 sample developed in this work, the four peaks still exist with similar positions but different ratios compared to Ta_2O_5-C. One noticeable feature is that the peak at 531 eV becomes dominant in Ta_2O_5, which indicates a high concentration of oxygen vacancies on its surface and reconfirms the EPR results. After integration with $IrRuO_x$, the O 1s spectra of

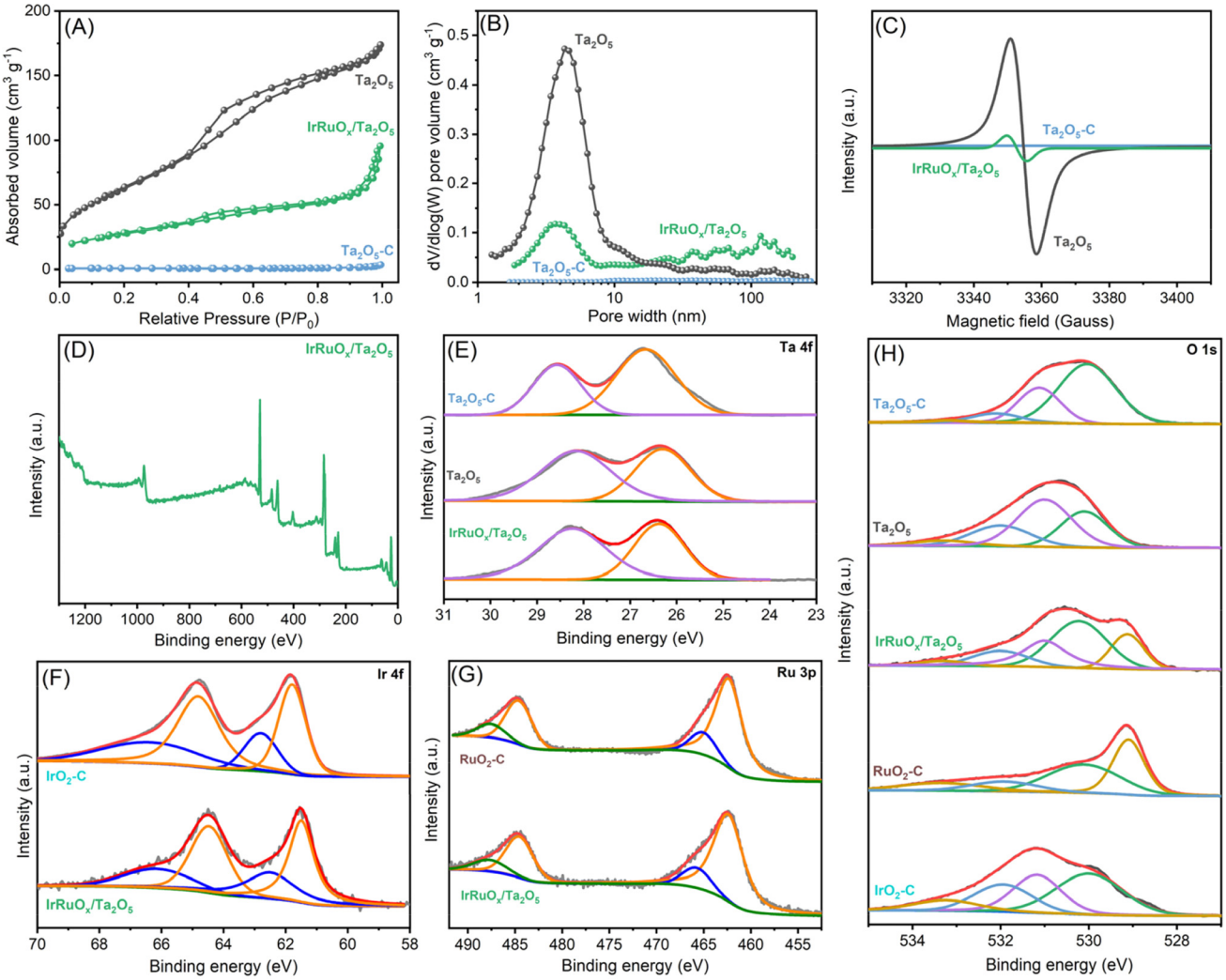

Fig. 3 (A) N_2 adsorption–desorption isotherms and (B) the resulting pore size distributions for the studied samples. (C) EPR spectra of the studied samples. (D) XPS full spectrum, (E) deconvoluted Ta 4f, (F) deconvoluted Ir 4f, (G) deconvoluted Ru 3p, and (H) deconvoluted O 1s spectra for the studied samples.

$IrRuO_x/Ta_2O_5$-C can be fitted into five peaks, centered at 529.1 eV, 530.2 eV, 531.0 eV, 532.0 eV, and 533.3 eV. By comparison with the peaks for IrO_2-C and RuO_2-C, it can be concluded that the peak at 529.1 eV in $IrRuO_x/Ta_2O_5$-C is assigned to the lattice O of RuO_2; the peak at 530.2 eV contains the lattice O of IrO_2, Ta_2O_5, and the hydroxyl species on Ru; and the peak at 531.0 eV still refers to vacant O, as confirmed by EPR. The aforementioned results indicate strong interactions between Ta and Ir, which could be due to the similar binding energies of lattice O in IrO_2 and Ta_2O_5.

To better understand how the loaded active species impacted the Ta_2O_5 support, we conducted synchrotron X-ray absorption characterization of $IrRuO_x/Ta_2O_5$. The standard Ta_2O_5 power sample and the Ta foil were also tested as references. Fig. 4A displays the X-ray absorption near edge structure (XANES) results to show the Ta-L3 edge of the samples. The peak intensity of the white line in the $IrRuO_x/Ta_2O_5$ catalyst is between Ta (Ta^0) and Ta_2O_5 (Ta^V), indicating that the average Ta oxidation state of the catalyst is between Ta^0 and Ta^V but closer to Ta^V. This observation agrees well with the XPS results. The Fourier transform extended X-ray absorption fine structure (EXAFS) spectra are shown in Fig. 4B–D, from which the local coordination environments of Ta can be interpreted. The bond length of Ta–O is 1.53 Å in the standard Ta_2O_5 sample. However, that length in $IrRuO_x/Ta_2O_5$ was determined to be 1.46 Å. Similar results were also observed from the wavelet transform EXAFS as shown in Fig. 4E–G. While the coordination number of Ta–O in $IrRuO_x/Ta_2O_5$ was close to 6 and similar to that in the Ta_2O_5 standard sample, the difference in the numbers of Ta–O in the first shell and the second shell still suggested different coordination configurations (Table S4, see the ESI†). Therefore, the decrease in the Ta–O bond length in $IrRuO_x/Ta_2O_5$ was mainly due to the interactions between Ta_2O_5 and $IrRuO_x$.[40]

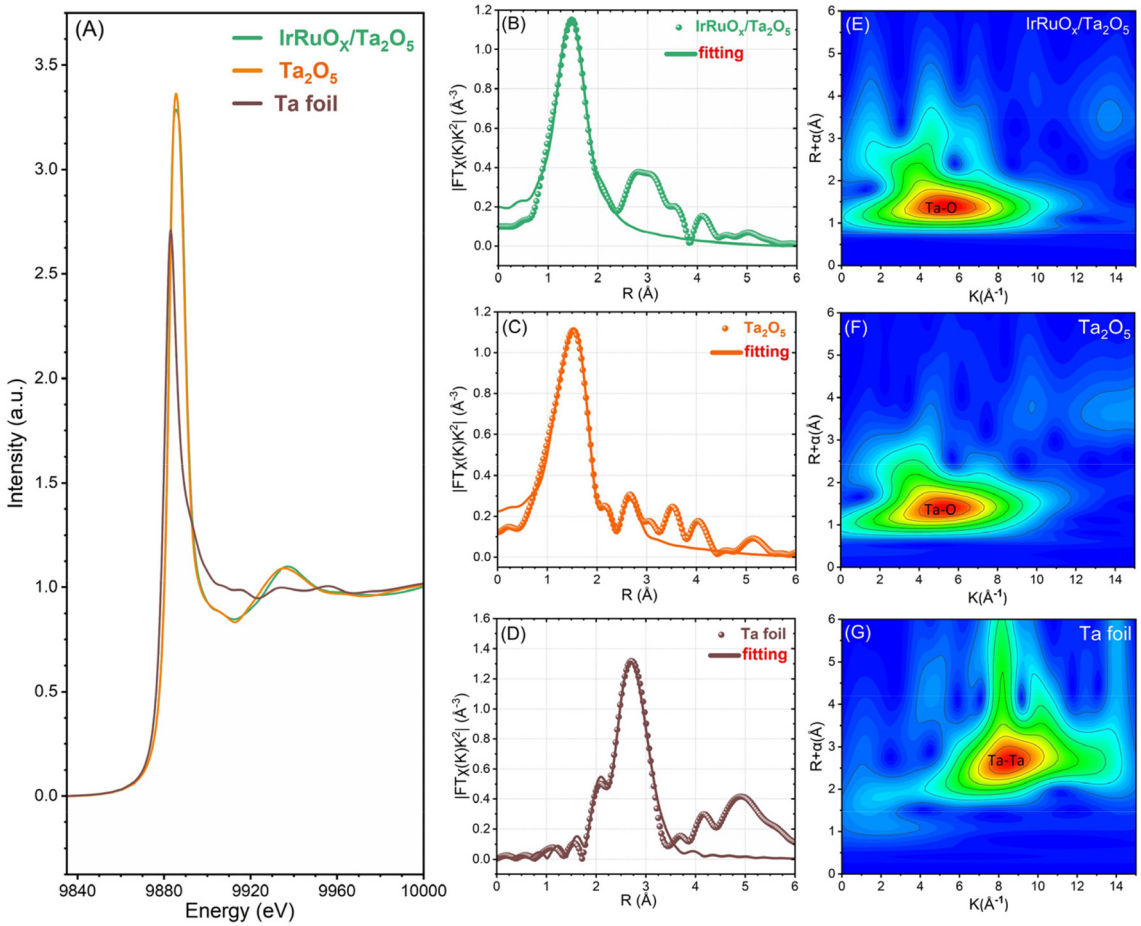

Fig. 4 (A) Ta L3-edge XANES spectra. FT-EXAFS spectra of (B) $IrRuO_x/Ta_2O_5$, (C) standard Ta_2O_5, and (D) Ta foil. WT-EXAFS spectra of (E) $IrRuO_x/Ta_2O_5$, (F) standard Ta_2O_5, and (G) Ta foil.

3.2 Electrochemical evaluation of the catalysts

To evaluate the OER catalytic responses of the studied samples, a mixture of the catalyst and ionomer was deposited onto the electrode surface with the catalyst loading precisely controlled. Linear sweep voltammetry (LSV) was first conducted for the electrodes with a total catalyst loading of 0.4 mg cm^{-2} in 0.5 M H_2SO_4 (Fig. 5A). Ta_2O_5 showed negligible OER activity but displayed a slight current improvement after integration with IrO_x. However, after integrating with RuO_x, the RuO_x/Ta_2O_5 sample had an excellent OER catalytic response and only needed an overpotential of 326 mV to deliver 10 mA cm^{-2}. After integration with both Ir and Ru, the OER catalytic activity of $IrRuO_x/Ta_2O_5$ significantly increased, and the overpotential decreased to 284 mV at 10 mA cm^{-2}. To understand whether the catalyst loading had a great impact on the catalytic performance, all catalysts with a total catalyst loading of 4 mg cm^{-2} were also evaluated under the same test conditions. Even at a high total catalyst loading of 4 mg cm^{-2}, the Ir loading of $IrRuO_x/Ta_2O_5$ was still fairly low (*ca.* 0.3 mg_{Ir} cm^{-2}). According to Fig. 5B, increasing catalyst loading did not help the Ta_2O_5 and IrO_x/Ta_2O_5 samples but further improved the OER catalytic activity of RuO_x/Ta_2O_5 and $IrRuO_x/Ta_2O_5$ with overpotentials of 240 mV and 235 mV at 10 mA cm^{-2}, respectively. We also adjusted the catalyst-to-support ratios to understand their impact on the catalytic performance of the OER. The results showed that $IrRuO_x/Ta_2O_5$ was optimal, and further increasing or decreasing the ratio suppressed the OER activity (Fig. 5C). To understand the OER kinetics, Tafel curves were plotted as shown in Fig. 5D. The Tafel slopes of IrO_x/Ta_2O_5, RuO_x/Ta_2O_5, and $IrRuO_x/Ta_2O_5$ were determined to be 94.2, 47.8, and 32.3 mV dec^{-1}, respectively, following the same trend as the OER voltammograms. With increasing current, $IrRuO_x/Ta_2O_5$, which had the smallest Tafel slope, had the smallest overpotential, confirming its excellent OER catalytic activity.

The electronic conductivity of the catalyst is critical for maximizing the participation of active sites in the OER. Therefore, the four studied samples were tested by electrochemical impedance spectroscopy (EIS), and the resulting curves are displayed in Fig. 5E. All four curves showed a similar starting point, which refers to the solution and connection resistance, indicating the reliability of the electrochemical testing system. The diameter of the semicircle in the high-frequency zone refers to the charge-transfer resistance of the catalyst. The diameter was the largest for both Ta_2O_5 and IrO_x/Ta_2O_5, decreased for RuO_x/Ta_2O_5, and the

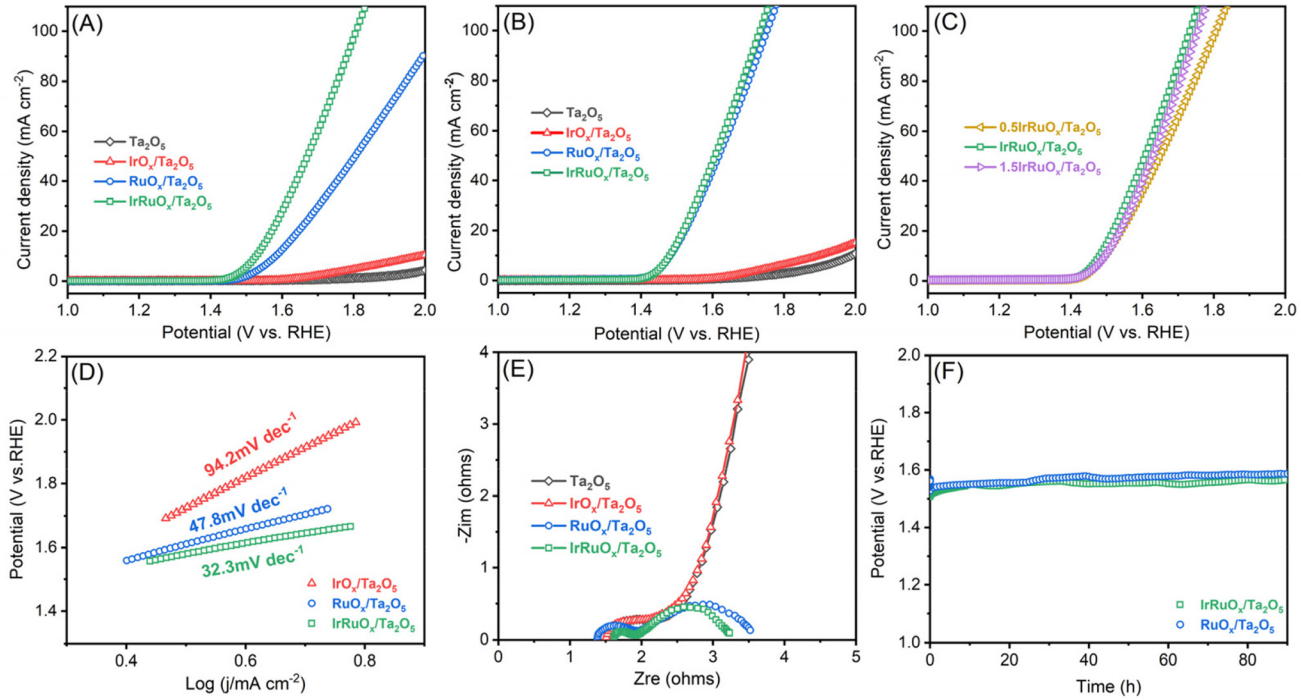

Fig. 5 OER LSV curves for the samples tested at (A) 0.4 mg cm^{-2} and (B) 4 mg cm^{-2}, and (C) different PGM/Ta ratios at 4 mg cm^{-2} in 0.5 M H_2SO_4. (D) Tafel plots derived from OER voltammograms recorded at 4 mg cm^{-2}. (E) EIS curves of the studied samples at 4 mg cm^{-2}. (F) Chronopotentiometric curves of 4 mg cm^{-2} $IrRuO_x/Ta_2O_5$ RuO_x/Ta_2O_5 at 10 A cm^{-2} for 90 h.

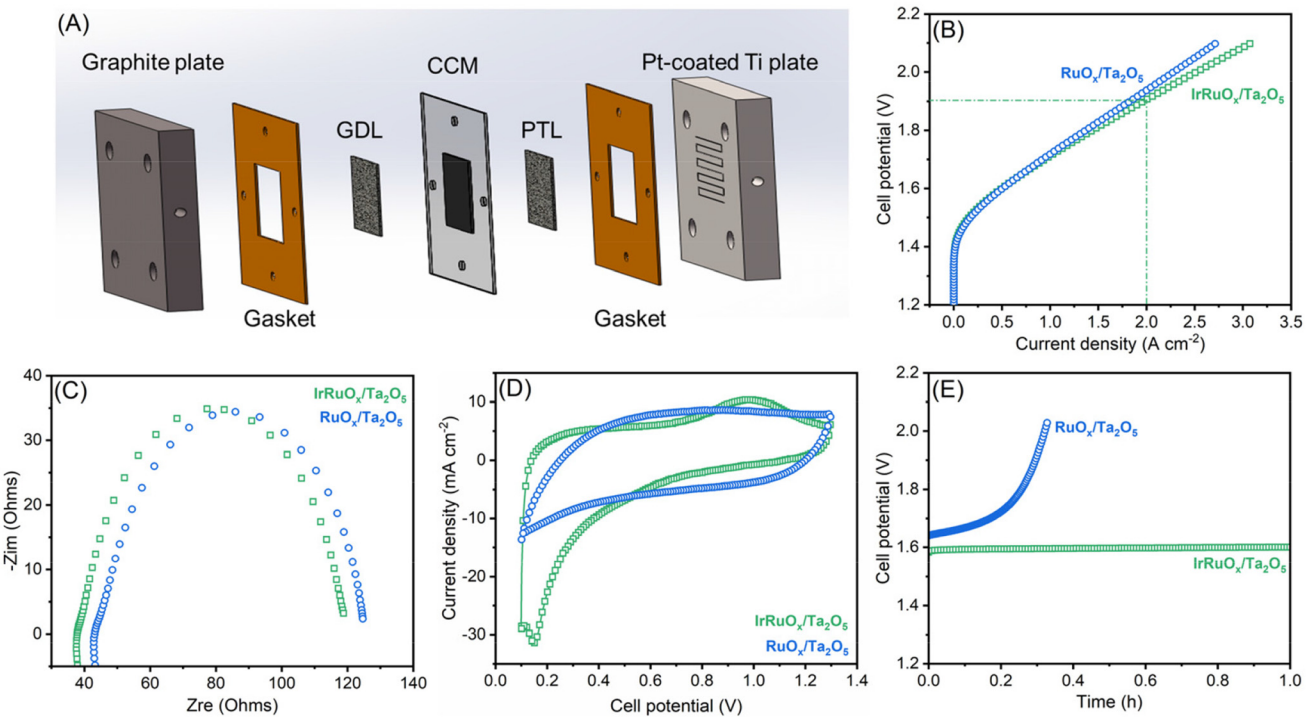

Fig. 6 (A) Scheme of a PEM water electrolyzer studied in this work. (B) Polarization curves, (C) EIS curves, (D) CV curves, and (E) chronopotentiometric curves at 500 mA cm^{-2} for $IrRuO_x/Ta_2O_5$ and $RuO_x/Ta_2O_{5_{m^4\ mg\ cm^{-2}}}$.

smallest for $IrRuO_x/Ta_2O_5$. The results suggested that $IrRuO_x/Ta_2O_5$ possessed the best electronic conductivity, which explained its excellent OER activity and fast kinetics. Adding RuO_x or $IrRuO_x$ actually decreased the electron transfer resistance of Ta_2O_5, suggesting that the catalyst was more charge conductive than the support. This also explains why the catalyst and support required an optimal ratio to afford the best catalytic activity (Fig. 5C). To understand how the loaded catalyst impacted the Ta_2O_5 double layer capacitance (C_{DL}), CV curves were recorded at different scanning speeds, and the results are shown in Fig. S5 (see the ESI†). The C_{DL} of Ta_2O_5 was determined to be 4.8 mF cm^{-2}, which improved to 56.3 mF cm^{-2} after integration with $IrRuO_x$, which explains the enhanced OER catalytic performance of $IrRuO_x/Ta_2O_5$. To understand the OER stability of the samples with and without Ir, chronopotentiometry was conducted at 10 mA cm^{-2} for RuO_x/Ta_2O_5 and $IrRuO_x/Ta_2O_5$. According to Fig. 5F, $IrRuO_x/Ta_2O_5$ maintained stable performance for up to 90 h, and RuO_x/Ta_2O_5 showed a slightly greater performance decay. Both catalysts have reasonable stabilities, benefiting from catalyst–support interactions, in half cells. The $IrRuO_x/Ta_2O_5$ catalyst developed in this work is among the best-performing Ta-supported catalysts reported in the literature as shown in Table S5 (see the ESI†).

The top two samples of $IrRuO_x/Ta_2O_5$ and RuO_x/Ta_2O_5 in half-cells were further evaluated in a PEM water electrolyzer. CCM was prepared and assembled with a cathodic gas diffusion layer and an anodic Ti felt porous transport layer, as schematically shown in Fig. 6A, and a photograph of CCM with gaskets is shown in Fig. S6 (see the ESI†). The catalyst loading for $IrRuO_x/Ta_2O_5$ was 4 mg cm^{-2} (*ca.* 0.3 mg_{Ir} cm^{-2}); and for 60 wt% Pt/C, the loading was 0.2 mg_{Pt} cm^{-2}. The *V–I* polarization curves were first recorded as shown in Fig. 6B. An electrolyzer with the $IrRuO_x/Ta_2O_5$ catalyst only needed 1.71 V to deliver 1 A cm^{-2} and 1.91 V to deliver 2 A cm^{-2}. However, the electrolyzer with the RuO_x/Ta_2O_5 catalyst needed higher cell potentials to deliver 1 A cm^{-2} (1.72 V) and 2 A cm^{-2} (1.94 V). Therefore, RuO_x/Ta_2O_5 showed less activity than $IrRuO_x/Ta_2O_5$, following the trend observed in half-cell tests. By comparing the EIS curves (Fig. 6C), it was found that both samples have a similar starting point and diameter of the semicircle, indicating a similar ohmic resistance in MEAs. The double layer capacitance between the catalyst and ionomer in the catalyst layer is important for enabling the participation of active sites in the OER. To evaluate this, cyclic voltammetry (CV) was conducted for both MEAs, and the resulting voltammograms in Fig. 6D indicate that the doping of Ir in RuO_x improved the electrochemically active surface area. The Ir dopants also improved the stability of the catalyst in MEA. Although RuO_x/Ta_2O_5 showed decent stability in a half cell at 10 mA cm^{-2}, it showed a fast performance decay when tested in MEA at 500 mA cm^{-2} (Fig. 6E).

4. Conclusion

In summary, a Ta_2O_5 support with an amorphous structure, a high surface area, and a high concentration of surface oxygen vacancies was synthesized by a facile method. After integration with the $IrRuO_x$ catalyst, strong interactions were found and they mainly occurred between Ir and Ta, and Ir became more electron-rich. In the $IrRuO_x$ active species, the doping of Ir in RuO_x improved the electrochemically active surface area and stability of RuO_x; therefore, $IrRuO_x/Ta_2O_5$ outperformed IrO_x/Ta_2O_5 and RuO_x/Ta_2O_5 in catalytic activity and stability. All the components in $IrRuO_x/Ta_2O_5$ worked synergistically to catalyze the OER so that a high loading of Ir was no longer needed. At 0.3 mg_{Ir} cm^{-2}, $IrRuO_x/Ta_2O_5$ only needed a 235 mV overpotential at 10 mA cm^{-2} in a half cell and a 1.91 V cell potential at 2 A cm^{-2} in a PEM water electrolyzer. This work opens up a new avenue for designing PEMWE catalysts supported by PGM-free metal oxides to reduce Ir loading while offering excellent activity and stability.

Conflicts of interest

There are no conflicts to declare.

Acknowledgements

This work was supported by the National Natural Science Foundation of China (no. 22308356), the Key R&D Program of Henan Province (no. 231111241800), Henan Provincial Science and Technology R&D Program Joint Fund (Advantageous Discipline Cultivation, no. 222301420045), Zhongke Technology Achievement Transfer and Transformation Center of Henan Province (no. 2024147), the Young Elite Scientists Sponsorship Program by CAST (no. 2021QNRC001), and the State Key Laboratory of Catalytic Materials and Reaction Engineering (RIPP, SINOPEC). The authors sincerely thank Prof. Suojiang Zhang (IPE, CAS) for his careful academic guidance and great support.

References

1 D. Guan, B. Wang, J. Zhang, R. Shi, K. Jiao, L. Li, Y. Wang, B. Xie, Q. Zhang, J. Yu, Y. Zhu, Z. Shao and M. Ni, *Energy Environ. Sci.*, 2023, **16**, 4926–4943.
2 A. M. Oliveira, R. R. Beswick and Y. Yan, *Curr. Opin. Chem. Eng.*, 2021, **33**, 100701.
3 B. Pivovar, N. Rustagi and S. Satyapal, *Electrochem. Soc. Interface*, 2018, **27**, 47.
4 D. Yao, L. Gu, B. Zuo, S. Weng, S. Deng and W. Hao, *Nanoscale*, 2021, **13**, 10624–10648.
5 M. Carmo, D. L. Fritz, J. Mergel and D. Stolten, *Int. J. Hydrogen Energy*, 2013, **38**, 4901–4934.
6 E. Fabbri and T. J. Schmidt, *ACS Catal.*, 2018, **8**, 9765–9774.
7 C. Minke, M. Suermann, B. Bensmann and R. Hanke-Rauschenbach, *Int. J. Hydrogen Energy*, 2021, **46**, 23581–23590.
8 Z. Lin, T. Wang and Q. Li, *Ind. Chem. Mater.*, 2023, **1**, 299–311.
9 K. Ayers, *Curr. Opin. Chem. Eng.*, 2021, **33**, 100719.

10 M. A. Hubert, L. A. King and T. F. Jaramillo, *ACS Energy Lett.*, 2022, **7**, 17–23.
11 Y. Lin, Y. Dong, X. Wang and L. Chen, *Adv. Mater.*, 2023, **35**, 2210565.
12 D. Escalera-López, S. Czioska, J. Geppert, A. Boubnov, P. Röse, E. Saraçi, U. Krewer, J.-D. Grunwaldt and S. Cherevko, *ACS Catal.*, 2021, **11**, 9300–9316.
13 J. Xu, J. Li, Z. Lian, A. Araujo, Y. Li, B. Wei, Z. Yu, O. Bondarchuk, I. Amorim, V. Tileli, B. Li and L. Liu, *ACS Catal.*, 2021, **11**, 3402–3413.
14 J. Zhang, X. Cao, Y.-F. Jiang, S.-F. Hung, W. Liu, H. B. Yang, C.-Q. Xu, D.-S. Li, T. Zhang, Y. Li, J. Li and B. Liu, *Chem. Sci.*, 2022, **13**, 12114–12121.
15 Y. Zheng, F. Zhang, G. Wang, D. Lai, L. Zou, Q. Cheng, J. Li, Z. Zou and H. Yang, *J. Power Sources*, 2022, **528**, 231189.
16 M. Bernt, A. Hartig-Weiß, M. F. Tovini, H. A. El-Sayed, C. Schramm, J. Schröter, C. Gebauer and H. A. Gasteiger, *Chem. Ing. Tech.*, 2020, **92**, 31–39.
17 A. S. Pushkarev, I. V. Pushkareva and D. G. Bessarabov, *Energy Fuels*, 2022, **36**, 6613–6625.
18 H. Chang, Z. Liang, L. Wang and C. Wang, *Nanoscale*, 2022, **14**, 5639–5656.
19 Z. Shi, X. Wang, J. Ge, C. Liu and W. Xing, *Nanoscale*, 2020, **12**, 13249–13275.
20 Y. Xu, K. Fan, Y. Zou, H. Fu, M. Dong, Y. Dou, Y. Wang, S. Chen, H. Yin, M. Al-Mamun, P. Liu and H. Zhao, *Nanoscale*, 2021, **13**, 20324–20353.
21 S. Zhao, A. Stocks, B. Rasimick, K. More and H. Xu, *J. Electrochem. Soc.*, 2018, **165**, F82.
22 G. Jiang, H. Yu, Y. Li, D. Yao, J. Chi, S. Sun and Z. Shao, *ACS Appl. Mater. Interfaces*, 2021, **13**, 15073–15082.
23 G. Jiang, H. Yu, D. Yao, Y. Li, J. Chi, H. Zhang and Z. Shao, *J. Mater. Chem. A*, 2022, **10**, 11893–11903.
24 T. L. Doan, H. E. Lee, M. Kim, W. C. Cho, H. S. Cho and T. Kim, *J. Power Sources*, 2022, **533**, 231370.
25 J. Cheng, J. Yang, S. Kitano, G. Juhasz, M. Higashi, M. Sadakiyo, K. Kato, S. Yoshioka, T. Sugiyama, M. Yamauchi and N. Nakashima, *ACS Catal.*, 2019, **9**, 6974–6986.
26 J. Zhang, Q. Zhang and X. Feng, *Adv. Mater.*, 2019, **31**, 1808167.
27 C. Han and T. Wang, *Energy Fuels*, 2023, **37**, 13624–13644.
28 W. Xiao, X. Huang, W. Song, Y. Yang, T. S. Herng, J. M. Xue, Y. P. Feng and J. Ding, *Nano Energy*, 2016, **25**, 60–67.
29 A. Liu, Z. Chen, X. Wei, W. Xiao and J. Ding, *MRS Commun.*, 2017, **7**, 563–569.
30 W. Xu, G. M. Haarberg, S. Sunde, F. Seland, A. P. Ratvik, E. Zimmerman, T. Shimamune, J. Gustavsson and T. Åkre, *J. Electrochem. Soc.*, 2017, **164**, F895.
31 F. Amano, Y. Furusho and Y.-M. Hwang, *ACS Appl. Energy Mater.*, 2020, **3**, 4531–4538.
32 C. Baik, J. Cho, J. I. Cha, Y. Cho, S. S. Jang and C. Pak, *J. Power Sources*, 2023, **575**, 233174.
33 J. Islam, B. S. Yoon, P. T. Thien, C. H. Ko and S.-K. Kim, *Catal. Today*, 2024, **425**, 114349.
34 Y. Liu, L. Xu, Y. Xin, F. Liu, J. Xuan, M. Guo and T. Duan, *J. Electrochem. Soc.*, 2022, **169**, 046516.
35 W. Li, J. Lv, D. Liu, W. Cai, X. Chen, Q. Huang, L. Wang and B. Wang, *Chem. Mater.*, 2023, **35**, 3892–3901.
36 H. Li, Y. Pan, L. Wu, R. He, Z. Qin, S. Luo, L. Yang and J. Zeng, *Int. J. Hydrogen Energy*, 2023, **48**, 26021–26031.
37 H.-S. Oh, H. N. Nong, T. Reier, A. Bergmann, M. Gliech, J. Ferreira de Araújo, E. Willinger, R. Schlögl, D. Teschner and P. Strasser, *J. Am. Chem. Soc.*, 2016, **138**, 12552–12563.
38 Z. L. Zhao, Q. Wang, X. Huang, Q. Feng, S. Gu, Z. Zhang, H. Xu, L. Zeng, M. Gu and H. Li, *Energy Environ. Sci.*, 2020, **13**, 5143–5151.
39 Z.-Y. Wu, F.-Y. Chen, B. Li, S.-W. Yu, Y. Z. Finfrock, D. M. Meira, Q.-Q. Yan, P. Zhu, M.-X. Chen, T.-W. Song, Z. Yin, H.-W. Liang, S. Zhang, G. Wang and H. Wang, *Nat. Mater.*, 2023, **22**, 100–108.
40 Y. Wang, H. Meng, M. He and H. Yu, *J. Alloys Compd.*, 2020, **822**, 153711.